# The Random Graph Model of Hydrogen Bond Network#

Masaki SASAI
Graduate School of Human Informatics, Nagoya University, Nagoya 464-01
(Received May 26, 1993)

A new lattice model of liquid water is developed. The hydrogen bond network is represented by the Ising variables with the method similar to the one used in combinatorial problems in random graph. Thermodynamic properties of the model are studies with the mean-field approximation. Phase diagram, density maximum, and anomalies of supercooled water are discussed. Dynamical properties are also investigated by using the coupled-map-dynamics method. Energy fluctuation is shown to have $1/f$ like long time correlation. The network structural rearrangement takes place collectively in localized regions.

Liquid water is a complex molecular system which shows many interesting dynamical and thermodynamic phenomena. Unusual dynamical behavior has been revealed by recent molecular dynamics (MD) studies; Amplitude of the potential energy fluctuation of each water molecule is much larger than the amplitude of the kinetic energy fluctuation.[1] Energy fluctuation shows $1/f$ like long time correlation at least in the frequency range of $10^0$—$10^3$ $cm^{-1}$ at room temperature.[2] Lifetime of hydrogen bond becomes anomalously large when temperature is lowered.[3] All these features come from the fact that water molecules are connected each other by hydrogen bond and form random and percolated network.[4,5] Individual water molecules embedded in this network can not move independently but should move collectively to rearrange the network structure. Then, how this collective motion is properly described ? How many molecules are involved in the motion ? How these motions are correlated in space and in time ? Such questions could be indeed important to understand dynamics of chemical reactions and relaxations in liquid water. Detailed MD investigations were performed to answer these questions[6,7] but they still remain to be open problems.

Intense interest has also been focused on the unusual behavior in statics of liquid water. Liquid water has exceptionally large specific heat, exhibits density maximum at 4 °C, and shows minimum in compressibility at 46 °C at atmospheric pressure. These peculiar properties, however, become more evident when liquid water is supercooled below the melting temperature. Especially significant is that thermodynamic response functions such as heat capacity, compressibility and expansivity tend to diverge at temperature around −45 °C at 1 atm.[8] Speedy gave a phenomenological explanation to this anomaly[9] by assuming that the spinodal line of the liquid–gas transition extends to the negative pressure region and is continuously connected to the instability line of the liquid–solid transition in the supercooled region. Then, thermodynamic response functions are expected to diverge approaching the liquid–solid instability line in the same way as they diverge around the liquid–gas spinodal line. Validity of Speedy's conjecture, however, is still under debate[10] and origin and nature of this anomaly remain to be open questions.

These dynamic and thermodynamic problems of liquid water are closely related to the combinatorial problem of the random graph. Figure 1 is a snapshot of the hydrogen bond network obtained from the MD calculation of liquid water. Hydrogen bond network is a random directed graph and the graph changes its topological shape due to the thermal fluctuation. In this work we develop a new lattice model of the random graph to investigate this structural rearrangement. The idea to represent the random graph by Ising spin Hamiltonian has been successfully applied to combinatorial problems,[11] such as the traveling salesman problem (TSP),[12,13] the weighted matching problem,[14] and the bi-partitioning problem.[15] In this paper the hydrogen bond graph is represented by a set of Ising spin variables in a manner similar to the method used in TSP and in the weighted matching problem.

In the next section the lattice model of the graph is introduced. This lattice-gas model is then studied with the mean-field approximation. Phase diagram and lines

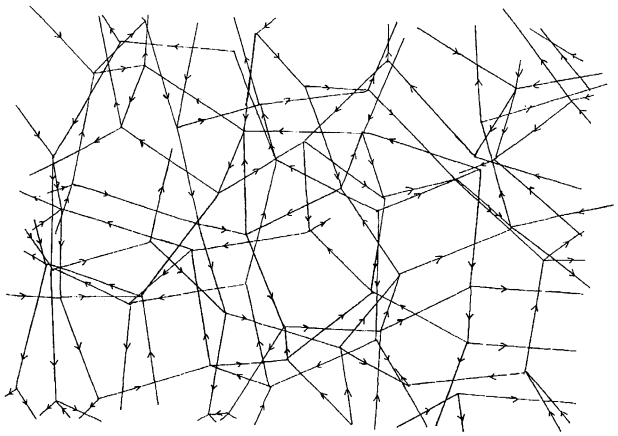

Fig. 1. A snapshort of the hydrogen bond network obtained from the molecular dynamics calculation. Arrow is directed from the hydrogen nucleus of one molecule to the oxygen nucleus of the other molecule.

#This paper is dedicated to the memory of Professor H. Kato.

of stability limit are derived and Speedy's conjecture is discussed. Then, in order to study dynamics of this lattice-gas model, we introduce a method similar to the one used by Hopfield and Tank to solve TSP.[12] Energy fluctuation and its power spectrum are calculated with this method and compared with the MD results. Final section is devoted to conclusion and discussion.

## The Lattice Model of Random Graph

Various types of lattice-gas models of water have been developed by different authors.[16—21] The same lattice, however, the body-centered-cubic (bcc) lattice has been used as the underlying lattice of models (Fig. 2a). When the half of the lattice sites are occupied by molecules, diamond structure is possible (Fig. 2b). Diamond structure is the structure of ice Ic. Physical properties of ice Ic is so close to the ones of the usual hexagonal ice, ice Ih, that ice Ic can be used as an approximation of ice Ih. When all the lattice sites are occupied, on the other hand, closely packed ice, ice VII or ice VIII should be formed. Thus the bcc lattice can represent as many phases as gas, liquid, open structured ice, and closely packed ice. In the present model we also use the bcc lattice as the underlying lattice framework.

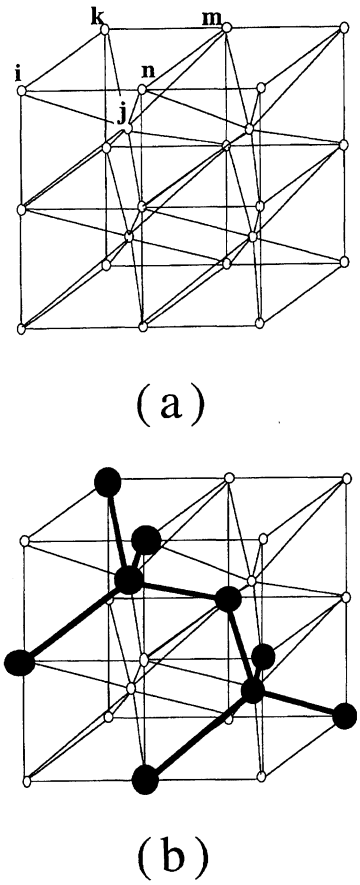


Fig. 2. (a) The body-centered-cubic (bcc) lattice used in the present model. The site $j$ is the nearest neighbor of the site $i$. The site $k$ and the site $n$ are 2nd neighbors and the site $m$ is the 3rd neighbor of the site $i$. (b) When the half of the bcc lattice sites are occupied, ice Ic which has the diamond structure can be formed.

We introduce the site variable $\sigma_i$ and the bond variable $s_{ij}$; $\sigma_i$ is defined on the $i$-th site and $s_{ij}$ is defined on the bond between the $i$-th site and its nearest neighbor $j$-th site. Both $\sigma_i$ and $s_{ij}$ are Ising variables with

$$\sigma_i = \begin{cases} 1 \text{ (when the } i\text{-th site is occupied by a molecule)} \\ 0 \text{ (otherwise)} \end{cases}, \quad (1)$$

and

$$s_{ij} = \begin{cases} 1 \text{ (when the O–H covalent bond is directed from the } i\text{-th site to the } j\text{-th site)} \\ 0 \text{ (otherwise)} \end{cases}, \quad (2)$$

Here we should note $s_{ij} \neq s_{ji}$ in general. See Fig. 3. We define the Hamiltonian

$$H = H_{\mathrm{CB}} + H_{\mathrm{HB}} + H_{\text{non-HB}}. \quad (3)$$

$H_{\mathrm{CB}}$ represents the condition that each water molecule has two O–H covalent bonds:

$$H_{\mathrm{CB}} = A \sum_i \left( \sum_j{}' s_{ij} - 2\sigma_i \right)^2, \quad (4)$$

where the primmed sum is a sum over nearest neighbors of the $i$-th site. $H_{\mathrm{CB}}$ is zero only when the condition $\sigma_i=1$, $\Sigma'_j s_{ij}=2$ or $\sigma_i=0$, $s_{ij}=0$ is satisfied. Any other configuration of $\sigma_i$ or $s_{ij}$ results in the nonzero value of $H_{\mathrm{CB}}$. When $H_3O^+$ and $OH^-$ are formed from $2H_2O$, for example, $H_{\mathrm{CB}}$ gives excess energy of $2A$. As a value of $A$, we could take $A \approx 11$ kcal mol$^{-1}$, because the energy to create the $H_3O^+$ and $OH^-$ pair in ice I is about 22 kcal mol$^{-1}$.[22] In later sections the larger value of $A$ than 11 kcal mol$^{-1}$ will be used in order to see the network rearrangement dynamics excluding the effect of the ionic pair formation. $H_{\mathrm{HB}}$ corresponds to hydrogen bond;

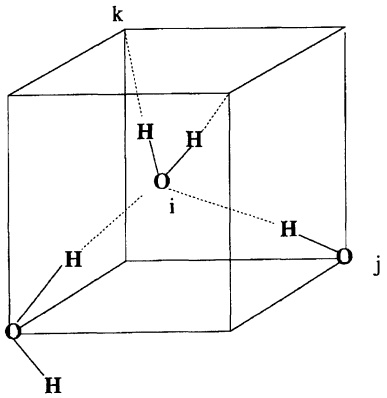


Fig. 3. With this configuration of molecules $\sigma_i=\sigma_j=1$ but $\sigma_k=0$. $s_{ik}=s_{ji}=1$ but $s_{ki}=s_{ij}=0$.

$$H_{\mathrm{HB}} = -\sum_i \sum_j{}' (Bs_{ij} - Cs_{ij}s_{ji})\,\sigma_i\sigma_j, \tag{5}$$

The term proportional to $B$ is the energy gain due to the hydrogen bond; $B \approx 4$ kcal mol$^{-1}$. The term proportional to $C$ represents the energy loss due to the repulsion between two hydrogen nuclei in the case O–H of one molecule and H–O of the other molecule come too close. $C$ is assumed to be $C \geq B$, so that the chance of formation of O–H--H–O configuration becomes small at low temperature. Thus, $A$ is assumed to be much larger than $B$ and $C$. $H_{\mathrm{non-HB}}$ is the part coming from the residual interactions other than hydrogen bond.

$$\begin{aligned} H_{\text{non-HB}} &= \frac{1}{2}\sum_i \sum_j{}' J_1\sigma_i\sigma_j + \frac{1}{2}\sum_i \sum_j{}'' J_2\sigma_i\sigma_j \\ &+ \frac{1}{2}\sum_i \sum_j{}''' J_3\sigma_i\sigma_j, \end{aligned} \tag{6}$$

where the summation with a prime is a sum over nearest neighbors, the one with double prime is a sum over 2nd neighbors and the one with triple prime is a sum over 3rd neighors. $J_1$, $J_2$, and $J_3$ include the van der Waals interactions and the Coulomb repulsion between Oxygen nuclei and typically less than 1 kcal mol$^{-1}$ at the distance farther than 3 Å.[22] Thus, $J_1$, $J_2$, and $J_3$ should be of order of thermal energy at room temperature but the energy in hydrogen bonding is much larger than that;

$$A \gg C \geq B \gg |J_1| \approx |J_2| \approx |J_3|. \tag{7}$$

These parameter values will be further calibratd in the next section so that the mean-field treatment gives reasonable results.

It is interesting to compare $H_{\mathrm{HB}}$ with the Hamiltonian of weighted matching problem;

$$H_{\mathrm{WMP}} = A\sum_i \left(\sum_j s_{ij} - 1\right)^2 + B\sum_i \sum_j r_{ij}s_{ij}, \tag{8}$$

where $r_{ij}$ is distance (weight) between the $i$- and $j$-th sites. When we pay attention to $s_{ij}$ and regard $\sigma_i$ as quenched variables in Eq. 3, several similarities between two Hamiltonians can be readily pointed out. Equation 8 was investigated in great detail by using the replica method which was developed in spin-glass problems.[14] The replica analysis suggests that the replica symmetric solution can describe the low temperature phase of the Hamiltonian (8), which means that the energy landscape is rugged but has no hierarchical structure. It would be a very interesting issue to investigate the energy landscape of the Hamiltonian (3) and compare it to the one of Eq. 8 or the TSP Hamiltonian.

## Mean Field Approximation

The grand canonical partition function, $\Xi$, for the Hamiltonian (3) is

$$\Xi = \sum_{\{\sigma\}} \sum_{\{s\}} \exp\left\{\left(-H + \mu\sum_i \sigma_i\right)\Big/ kT\right\}, \tag{8}$$

Where $\Sigma_{\{\sigma\}}$ and $\Sigma_{\{s\}}$ are summation over configurations of $\sigma_i$ and $s_{ij}$ and $\mu$ is the chemical potential. Grand potential $\Omega$ is $\Omega = -PV = -kT\log \Xi$. First, the summation over $s_{ij}$ is carried out in an approximate way. In this summation the assumption of no ionic pair ($A \to \infty$) is used. Detailed explanation of this approximate sum is given in Appendix. After this summation, we have the effective Hamiltonian

$$\begin{aligned} \Xi &= \sum_{\{\sigma\}} \exp\{-H_{\mathrm{eff}}/kT\}, \\ H_{\mathrm{eff}} &= \Psi(T, \{\sigma_{ij}\}) + H_{\text{non-HB}} - \mu\sum_i \sigma_i, \end{aligned} \tag{9}$$

where $\Psi(T, \{\sigma_i\})$ is

$$\begin{aligned} &\Psi(T, \{\sigma_i\}) = \\ &-kT\sum_i \sigma_i \log\left\{\frac{1}{2}\left[8 + \chi\sum_j{}'\sigma_j\right]\left[7 + \chi\sum_j{}'\sigma_j\right]\right\}, \end{aligned} \tag{10}$$

and

$$\chi = \exp\left\{\frac{1}{kT}\left[B - (C/4)\exp\left(\frac{B-C}{kT}\right)\right]\right\} - 1. \tag{11}$$

The similar technique has been used in Ising–Potts spin system[20,23] to obtain the effective Ising Hamitonian by tracing out the Potts variables. The functional form of $\Psi(T, \{\sigma_i\})$ is shown in Fig. 4. $\Psi(T, \{\sigma_i\})$ which comes from the degree of freedom of $s_{ij}$ is an attractive potential and has the form of the entropic force. At high temperature $s_{ij}$ can take more configurations than at low temperature. In other words, the entropy gain due to the rotational degree of freedom is the source of this attractive force. This mechanism is quite similar to that found in the Ising–Potts lattice model of water by Sastry et al.[20]

In this paper we will not consider the closely packed ice but concentrate on three low density phases; gas, liquid, and open ice. In order to treat the open ice phase, we divide the bcc lattice into four sub-lattices, the lattice-1,2,3, and 4. In Fig. 5 these sub-lattices are designated with four different symbols. By using the mean-field approximation, the grand potential is written with the sub-lattice densities $\sigma_1$, $\sigma_2$, $\sigma_3$, and $\sigma_4$,

$$\begin{aligned} \Omega = N\Big\{&-\frac{T}{2}(\sigma_1 + \sigma_2) \\ &\times \log\left\{\frac{1}{2}[4\chi(\sigma_3 + \sigma_4) + 8][4\chi(\sigma_3 + \sigma_4) + 7]\right\} \\ &- \frac{T}{2}(\sigma_3 + \sigma_4) \end{aligned}$$

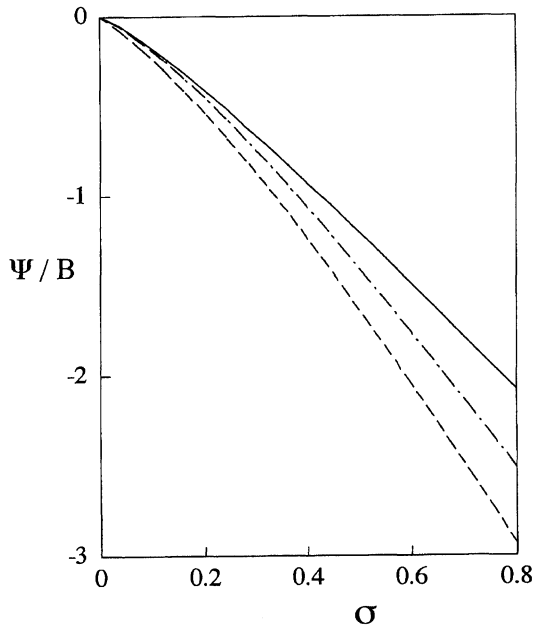


Fig. 4. The functional form of the effective potential $\Psi(T, \{\sigma_i=\sigma\})$ is shown at temperature $T/B=0.2$ (—), $T/B=0.4$ (-·-), and $T/B=0.6$ (---). $\Psi$ is scaled by the energy parameter of hydrogen bond $B$. $\Psi$ is the attractive force (it decreases as density increases). $C/B=2$ is used.

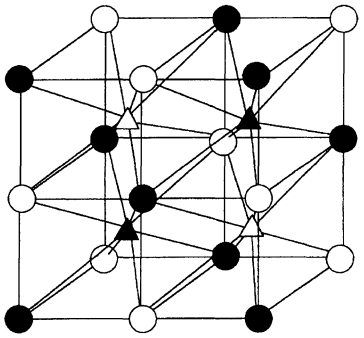

Fig. 5. In the mean-field calculation, the bcc lattice is divided to four sub-lattices, lattice-1 ○, lattice-2 ●, lattice-3 △, and lattice-4 ▲.

$$\times \log\left\{\frac{1}{2}\left[4\chi\left(\sigma_1+\sigma_2\right)+8\right]\left[4\chi\left(\sigma_1+\sigma_2\right)+7\right]\right\}$$
$$+\frac{z_1J_1}{4}\left(\sigma_1+\sigma_2\right)\left(\sigma_3+\sigma_4\right)+\frac{z_2J_2}{2}\left(\sigma_1\sigma_2+\sigma_3\sigma_4\right)$$
$$+\frac{z_3J_3}{4}\left({\sigma_1}^2+{\sigma_2}^2+{\sigma_3}^2+{\sigma_4}^2\right)$$
$$-\frac{\mu}{2}\left(\sigma_1+\sigma_2+\sigma_3+\sigma_4\right)\Big\}-TS, \qquad (12)$$

where $z_1$ is the number of nearest neigbors, $z_1=8$, $z_2$ the number of 2nd neighbors, $z_2=6$, and $z_3$ the number of 3rd neighbors, $z_3=4$. The number of the bcc lattice sites is $2N$ (the number of unit cells is $N$). $S$ is the mean-field expression of entropy,

$$S=\frac{N}{2}\sum_{\lambda=1}^{4}\left\{\sigma_\lambda\log\sigma_\lambda+\left(1-\sigma_\lambda\right)\log\left(1-\sigma_\lambda\right)\right\}, \qquad (13)$$

Here we define $n$, $m$, $l$, and $k$ by the linear combination of $\sigma_1$, $\sigma_2$, $\sigma_3$, and $\sigma_4$.

$$\begin{aligned} n &= \left(\sigma_1+\sigma_2+\sigma_3+\sigma_4\right)/4, \\ m &= \left(\sigma_1-\sigma_2+\sigma_3-\sigma_4\right)/4, \\ l &= \left(\sigma_1-\sigma_2-\sigma_3+\sigma_4\right)/4, \\ k &= \left(\sigma_1+\sigma_2-\sigma_3-\sigma_4\right)/4, \end{aligned} \qquad (14)$$

$n$ is the average density of molecules and $m$, $l$, and $k$ are order parameters of the symmetry breaking transitions. $n$, $m$, $l$, and $k$ satisfy

$$\frac{\partial\Omega}{\partial n}=\frac{\partial\Omega}{\partial m}=\frac{\partial\Omega}{\partial l}=\frac{\partial\Omega}{\partial k}=0, \qquad (15)$$

Eq. 15 has the following types of solutions,

$$\begin{aligned} &\text{gas;}\quad (n=n_g, m=l=k=0) \\ &\text{liquid;}\quad (n=n_1, m=l=k=0) \\ &\text{ice;}\quad (n=n_s, m=\pm d_s, l=k=0) \\ &\text{or}\quad (n=n_s, l=\pm d_s, m=k=0), \end{aligned} \qquad (16)$$

Four degenerated solutions for ice in Eq. 16 are physically equivalent.

## Density Maximum, Phase Diagram, and Stability Limit

In Fig. 6 we show the temperature dependence of density $n$ in the liquid phase under constant pressure, which is obtained by solving Eqs. 12, 13, 14, and 15. Larger the pressure, lower the temperature of the density maximum. The attractive force $\Psi(T, \{\sigma_i\})$ of Eq. 10 plays an essential role for the system to exhibits this density maximum. In high enough temperature entropy of Eq. 13 becomes dominant, so that density decrease as temperature is increased. In lower temperature $\Psi(T, \{\sigma_i\})$ becoems more significant and density becomes larger with this attractive potential. Further lowering temperature, however, the strength of $\Psi(T, \{\sigma_i\})$ decreases (see Fig. 4) and is overcome by the repulsive term in $H_{\text{non-HB}}$, so that density decreases again.

The liquid–gas coexistence line is obtained by equating the grand potential as $\Omega\ (n=n_g,\ m=l=k=0)=\Omega\ (n=n_1,\ m=l=k=0)$. The coexistence line between liquid and ice and the line between gas and ice can be similarly obtained by equating the grand potential. Thus obtained phase diagram is shown in Fig. 7. The gas–liquid coexistence line is terminated by the critical point. The slope of the liquid–ice coexistence line is negative as observed in real water.

Stability limit of the liquid phase is obtained by solving the equation for the 4×4 matrix $\partial^2\Omega/\partial\sigma_\lambda\partial\sigma_\mu$ with $\lambda$, $\mu$=1, 2, 3, or 4,

$$\det\left\{\frac{\partial^2\Omega}{\partial\sigma_\lambda\sigma_\mu}\right\}=0, \qquad (17)$$

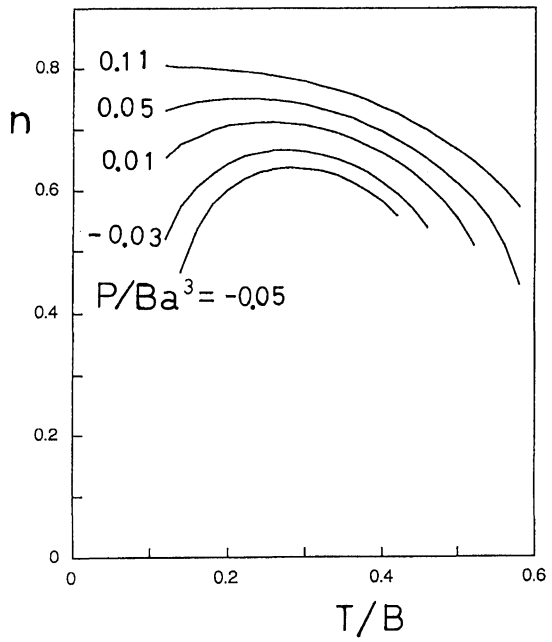


Fig. 6. Temperature dependence of density $n$ in the liquid phase at various pressures. Temperature $T$ is scaled by the energy parameter of hydrogen bond $B$ and pressure $P$ is scaled by $Ba^3$, where $a^3$ is the volume of the unit cell of the bcc lattice. Parameters are $C/B=2$, $J_1/B=0.12$, $J_2/B=0$, and $J_3/B=-0.2$.

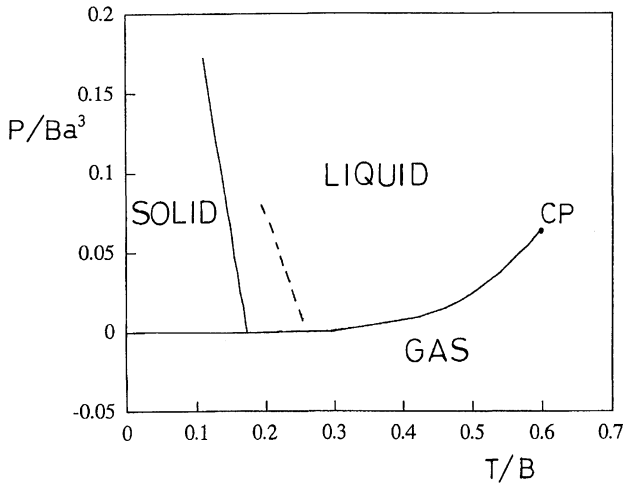


Fig. 7. The mean-field phase diagram. CP is the critical point and the dashed line is the line where density becomes maximum. The same parameters are used as in Fig. 6.

Thus derived lines of the stability limit is shown in Fig. 8. There are two instability lines. One is the spinodal line for the transition from liquid to gas. This line starts from the critical point and, as lowering temperature, extends into the negative pressure region. Then it changes its sign of slope, showing the bending point. The line of density maximum approaches this bending point as predicted from the thermodynamic consistency argument.[9,24] The bending point is, thus, the point that

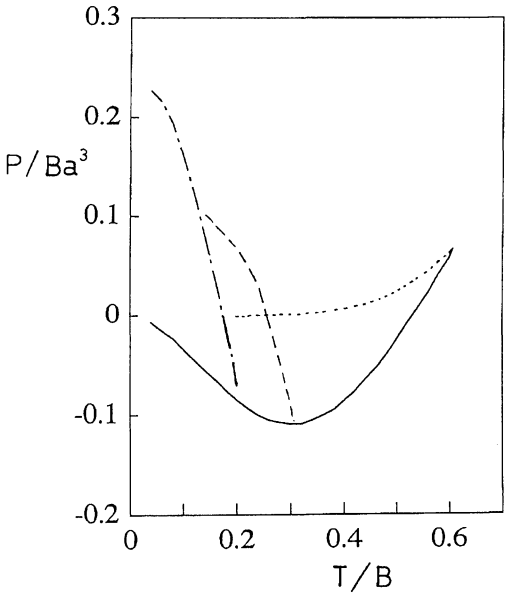


Fig. 8. The instability line (spinodal line) for the transition from liquid to gas (—), the instability line for the transition from liquid to ice (–·–), the liquid–gas coexistence line (····), and the line of density maximun (- - -). The line of density maximum approaches to the bending point of the liquid-gas instability line at around $P/Ba^3=-0.1$. The same parameters are used as in Fig. 6.

the attractive force of $\Psi(T, \{\sigma_i\})$ and the repulsive force in $H_{\text{non-HB}}$ are balanced. There is another line of the stability limit. This is the instability line for the transition from liquid to ice. This instability arises from the competition between $\Psi(T, \{\sigma_i\})$ and $H_{\text{non-HB}}$. The line approaches close to the bending point of the liquid-gas spinodal.

In Fig. 9 both the instability line of the liquid–ice transition and the liquid–ice coexistence line are shown with the enlarged scale. Two lines lie very close to each other and the metastable supercooled region is narrow. This may be due to the simplified Hamiltonian structure we used in our model and a remedy would be to use the more realistic Hamiltonian; If the three- or more-body molecular interaction can be effectively taken into account in $H_{\text{HB}}$, then the ice phase might be more stabilized and the metastable supercooled region would be enlarged. For the sake of simplicity, however, we do not go into this point further in the present work.

Recently Sastry et al. developed the Ising–Potts lattice model of water and showed that the mean-field behavior of the model agrees with Speedy's conjecture in many points.[20] In their model the liquid–ice instability line is tangentially connected to the liquid–gas instability line. This is due to the high symmetry of their model Hamiltonian. In the present model without such symmetry, two lines come close around the bending point but are not continuously connected. We have two lines of the different nature and the thermo-

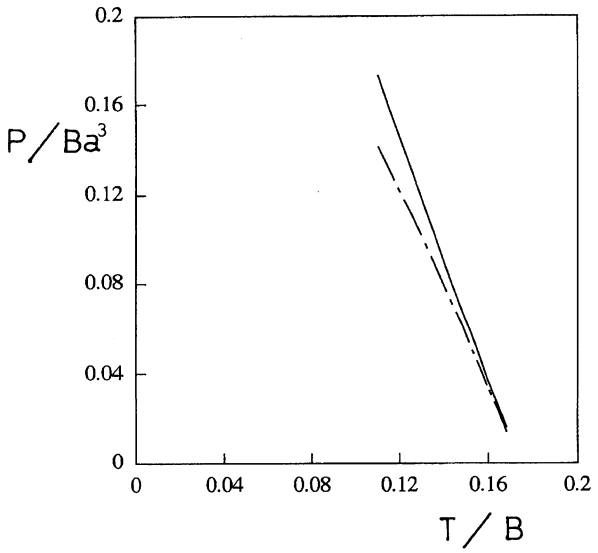


Fig. 9. The liquid–ice coexistence line (——) and the liquid-ice instability line (– · –) lie closely in the $T$–$P$ plane in the present model. The same parameters are used as in Fig. 6.

dynamic behavior near the liquid–ice instability line is not necessarily same as the divergent behavior around the liquid–gas instability line. With the present mean-field treatment $(\partial P/\partial n)_T=0$ at the liquid–gas instability line, so that compressibility diverge near this line. At the liquid–ice instability line, $(\partial P/\partial m)_T=0$ but $(\partial P/\partial n)_T\neq 0$, therefore compressibility does not diverge around this line. This result of no divergence, however, could be due to the artifact of the mean-field approximation and is not the conclusive result for this lattice model. In fact, the functional integral treatment of the lattice model[7,25] predicts that thermodynamic response functions diverge around both two instability lines. This important issue will be discussed in the subsequent publication.[26]

## Coupled Map Dynamics of the Random Graph

In the following part of this paper we discuss dynamics of this lattice model. A merit to utilize the present lattice model to study the dynamical network structural change is the simplicity that the network is directly represented by the variable $s_{ij}$. This would make the analysis easier than the MD simulations in which the network must be "defined" through the orientation or other properties of molecules or by using the quenching method.[6,27]

MD calculations have shown that (1); the rotational motion of molecule is more than several times faster than the translational motion, and (2); translation and rotation are not independent separate motions but translation takes place in concert with rotation.[1,6] In order to capture these features, we here use the coupled-map-dynamics technique;[28] We regard $s_{ij}$ as the variable which takes a continuous real value. This is the "soft spin" technique developed by Oono and Puri for the lattice-gas dynamics of the spinodal decomposition[28] and by Hopfield and Tank for the neural network implementation of TSP.[12] $s_{ij}$ of the next time step is calculated by using the following rule;

$$\begin{aligned} u_{ij}(t+\delta t) &= s_{ij}(t) - \eta\frac{\partial H}{\partial s_{ij}(t)} + \xi_{ij}(t), \\ s_{ij}(t+\delta t) &= F\left(u_{ij}(t+\delta t)\right), \end{aligned} \tag{18}$$

where $\xi_{ij}(t)$ is the Gaussian random number which has the following expectation values:

$$\begin{aligned} &\langle \xi_{ij}(t)\rangle = 0, \\ &\langle \xi_{ij}(t_1)\xi_{mn}(t_2)\rangle = 2\eta kT\delta_{im}\delta_{jn}\delta_{t_1t_2}, \end{aligned} \tag{19}$$

and $F(u)$ is a sigmoidal function which connects 0 and 1 as shown in Fig. 10. Here we use $F(u)$ of the following form:[28]

$$F(u) = \begin{cases} 1 & (\text{for } u > 1) \\ \dfrac{\omega(2u-1)}{2\sqrt{1+(2u-1)^2(\omega^2-1)}} + \dfrac{1}{2} & \\ & (\text{for } 1 \geq u \geq 0) \\ 0 & (\text{for } 0 > u) \end{cases}, \tag{20}$$

The map $u(n+1)=F(u(n))$ has three fixed points at $u=0$, 0.5, and 1. The fixed point at 0.5 is unstable but the fixed points at 0 and 1 are stable. Thus, by repeatedly applying Eq. 18, $s_{ij}$ tends to converge to 0 or 1. Equation 18 is used as the parallel updating rule applied to every bond variable at the same time and the periodic boundary condition is used. The larger the values of $\omega$ and $\eta$, the higher the computational efficiency. But when $\omega$ or $\eta$ exceeds the threshold value, Eq. 18 becomes unstable against the strong oscillation or is frozen to some fixed configuration,[28] In order to avoid these

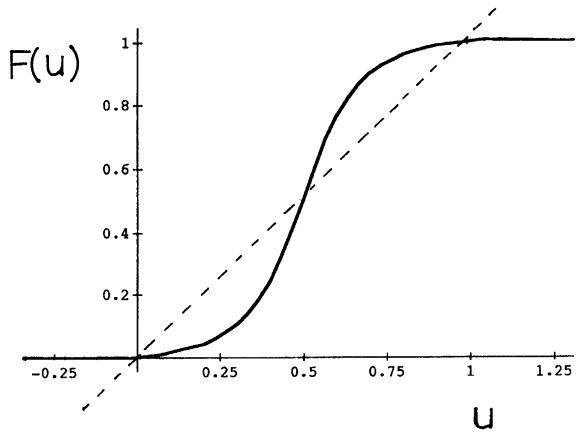


Fig. 10. A sigmoidal function $F(u)$ of Eq. 20 with $\omega=3$ is shown. It has three crossing points with the line $u=F(u)$ at $u=0$, 0.5, and 1.

numerical instabilities, we use rather moderate values, $\omega=1.2$ and $\eta=0.01$ in the present calculation.

Translational motion is calculated by using the Kawasaki exchange rule. The site $i$ is randomly selected and then one of its nearest or 2nd neighors $j$ is randomly chosen. If $\sigma_i=0$ and $\sigma_j=1$, or if $\sigma_i=1$ and $\sigma_j=0$, the value of $\sigma_i$ and the value of $\sigma_j$ are exchanged as a trial. Then the rule (18) is applied several times. It was found that 10 times application of (18) is enough for the convergence of $s_{ij}$ at low temperature liquid phase. The energy is calculated with this trial configuration of $\{\sigma_i\}$ and $\{s_{ij}\}$, and this trial is accepted or rejected following the usual Metropolis judgement. 1 Monte Carlo step (1MCS) is defined as $2N$ trials.

At temperature around the mean-field liquid–ice instability line, the application of Eq. 18 almost always bring $\{s_{ij}\}$ to the configuration of its nearest energy minimum. Figure 11 schematically shows this situation. When $\{\sigma_i\}$ is fixed, the energy landscape for $\{s_{ij}\}$ has many local minima corresponding to many possible network configurations. Following Eq. 18, $\{s_{ij}\}$ finds one of its local minimum. When $\{\sigma_i\}$ is changed with the Kawasaki rule, the energy landscape is modified and $\{s_{ij}\}$ is driven to the newly formed energy minimum. We regard MCS as a unit of "time" $t$. Thus, "temporal" changes in energy and in structure of the network are investigated with this Kawasaki-coupled map method.

### 1/*f*- like Long Time Energy Fluctuation

Figure 12 is a snapshot of the network structure calculated with the above method. We can see the spatial fluctuation in the network density. There are close-packed dense regions and bond-breaking sparse regions. These regions change their boundaries as time proceeds in our dynamics.

Figure 13 is the temporal variation of the energy fluctuation $\Delta E$:

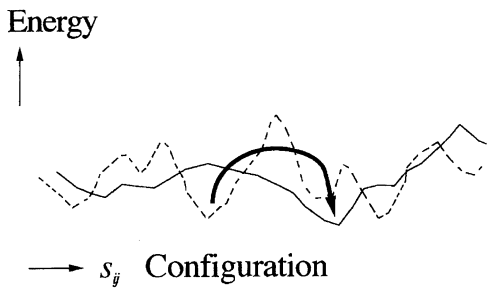


Fig. 11. Schematic representation of the dynamics. When we regard $\{\sigma_i\}$ as quenched variable, the energy landscape for $\{s_{ij}\}$ is rugged corresponding to the many possible ways to connect bonds among molecules. The network structure trapped in one of the local energy minimum is moved by the modification of the energy landscape with the slow translational motion.

$$\Delta E(t) = H_{\text{HB}}(t) + H_{\text{non-HB}}(t) - \langle H_{\text{HB}} + H_{\text{non-HB}} \rangle, \quad (21)$$

where $<\cdots>$ is the average taken along the trajectory. In Fig. 13 we can see that there are multiple timescales; $\Delta E$ is described as the superposition of rapid oscillations and slow variations. This multiplicity in timescale can be quantitatively represented by the power spectrum $S(f)$:

$$S(f) = \left| \sum_t \Delta E(t) e^{2\pi i f t} \right|^2 . \quad (22)$$

If $\Delta E$ is described by the single relaxation-time constant

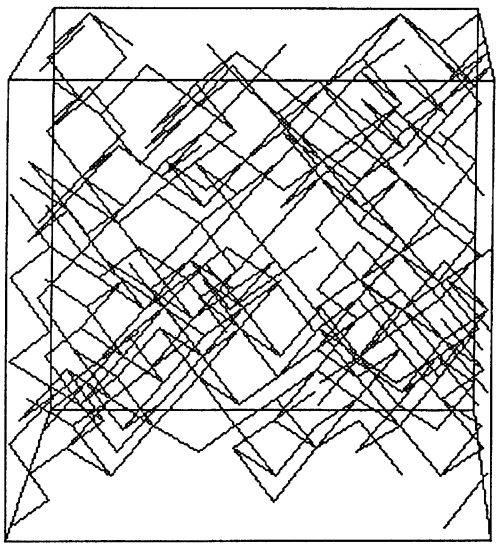

Fig. 12. A snapshot of the network structure in the present lattice model. Real lines are drawn where $\sigma_i\sigma_i s_{ij} > 0.8$. The lattice size $2N=2\times6\times6\times6$, the number of molecules is 259 and temperature is $T/B=0.1$. Parameters are $A/B=10$, $C/B=1$, $J_1/B=-0.05$, $J_2/B=0.1$, and $J_3/B=0$.

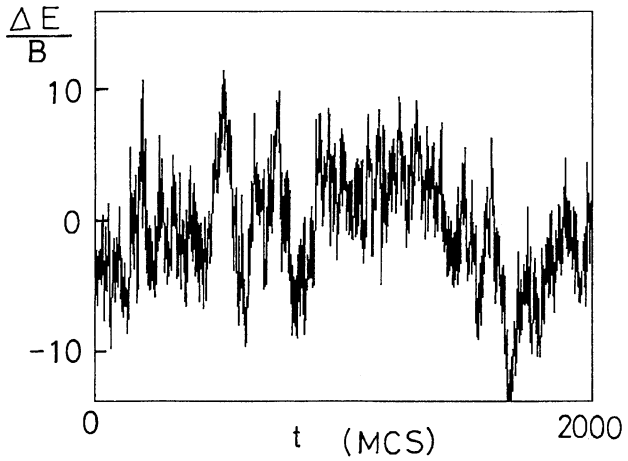


Fig. 13. The energy fluctuation $\Delta E$ is shown along the trajectory of the dynamics. $T/B=0.1$ and the lattice size, the number of molecules and energy parameters are same as in Fig. 12.

$\tau$ (in other words, if $\Delta E$ follows the Debye relaxation law), then $S(f)$ must be a Lorentzian.

$$S(f) \propto \frac{\tau}{1+(2\pi\tau f)^2}. \tag{23}$$

Figure 14 is the power spectrum obtained from the data of Fig. 13. The spectrum is well fitted by $f^{-1.5}$ and far different from the Lorentzian; The energy fluctuation of this model does not follow the usual Debye relaxation law.

The similar spectrum has been obtained in the MD calculation of water;[2] By filtering out samll amplitude oscillations with the quenching technique, the power spectrum of the energy flucturation in the MD calculation was shown to be approximately $f^{-1.3}$ at room temperature. The exponent becomes larger than 1.3 when temperature is lowered.[2]

The fluctuation which has the power spectrum of $f^{-\alpha}$ with $0<\alpha<2$ is so called $1/f$ or flicker noise. Many systems have been known to exhibit this $1/f$ noise and thus various mechanisms have been considered.[29] One possible interpretation is that the power spectrum is the superposition of Lorentzian spectra with the weight $g(\tau)$,

$$S(f) = \int \mathrm{d}\tau \frac{g(\tau)\tau}{1+(2\pi\tau f)^2}. \tag{24}$$

$g(\tau)$ is the distribution function of relaxation-time constants and $g(\tau)\approx\tau^{-0.5}$ to yield the $f^{-1.5}$ spectrum. Such broad distribution of relaxation-time constants is in strong contrast with the very narrow distribution of time constants observed in dielectric relaxation measurements in liquid water.[22] This might be because in the dielectric relaxation measurement information on the non-Debye component of relaxation is lost by observing the averaged polarization vector. The present results suggest that the meaning of "average" in the experimental measurement should be examined more carefully. Further analysis on the difference between the energy relaxation and the dielectric relaxation is needed.

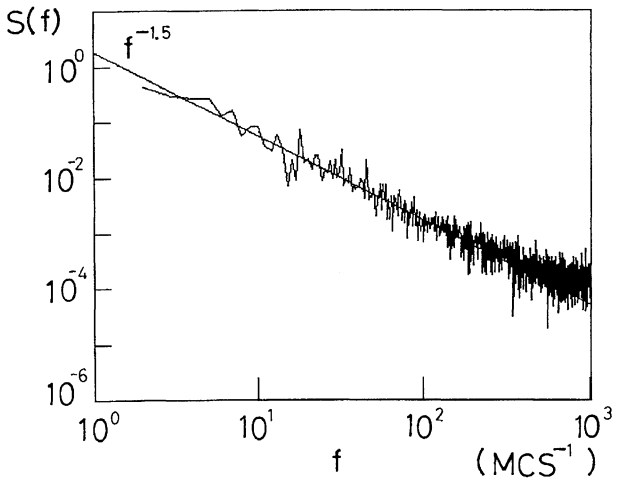


Fig. 14. The power spectrum $S(f)$ obtained from the Fourier transformation of the data in Fig. 13.

Equation 24 has often been used to interprete $1/f$ noise as the superposition of many activation processeses with the broad distribution of activation energy.[29] In the present model, however, there is no theoretical justification to assume such broad distribution of activation energy. The origin of $1/f$ noise shown in Fig. 14 is, thus, still an open problem. One way to look at this problem is to analyze the relation between the temporal scaling behavior and the spatial fluctuation of the network structure. Here we take a glance at this problem by showing the representative patterns of the hydrogen bond rearrangement in Fig. 15. We can see that the network rearrangement occurs in some localized regions. These regions often have interesting shapes such as the string-like shape or the two dimensional sheet-like form. Dynamics of this model with the larger number of lattice sites is now being studied to analyze the distribution of size and shapes of these regions.

## Conclusions

In this paper a new lattice model of the hydrogen bond network was developed. The random hydrogen bond network is represented by the Ising spin Hamiltonian. This Hamiltonian has the structure similar to those used to solve the combinatorial problems in random graph.

Thermodynamic properties of this model were studied with the mean-field approximation and it was shown that the present model has properties similar to the features of real water. The liquid–gas spinodal line has a bending point in the $T$–$P$ plane at the negative pressure. The line of density maximum reaches this bending point as was expected from the thermodynamics consistency. There is another line of instability for transition from liquid to ice. This liquid–ice instability line extends near to the bending point of the liquid–gas spinodal line but two lines are not continuously connected. The existence of the bending point agrees with Speedy's conjecture but it does not necessarily mean that the system behaves in the same way around the liquid-gas instability line and around the liquid-ice instability line. The thermodynamic behavior around the liquid–ice instability must be more deeply studied with the approximation beyond the mean-field treatment of this paper.

Dynamics of this model were investigated with the new method which is the combination of the coupled map dynamics rule for rotation and the Kawasaki exchange rule for translation. The energy fluctuation yields the $1/f^{1.5}$ power spectrum with very long time correlation. Thus, the energy fluctuation of the present model can not be described by the single relaxation-time constant. This multiplicity of timescales should be due to the multiplicity of the network structures and of the pathways to rearrange the network. The spatial

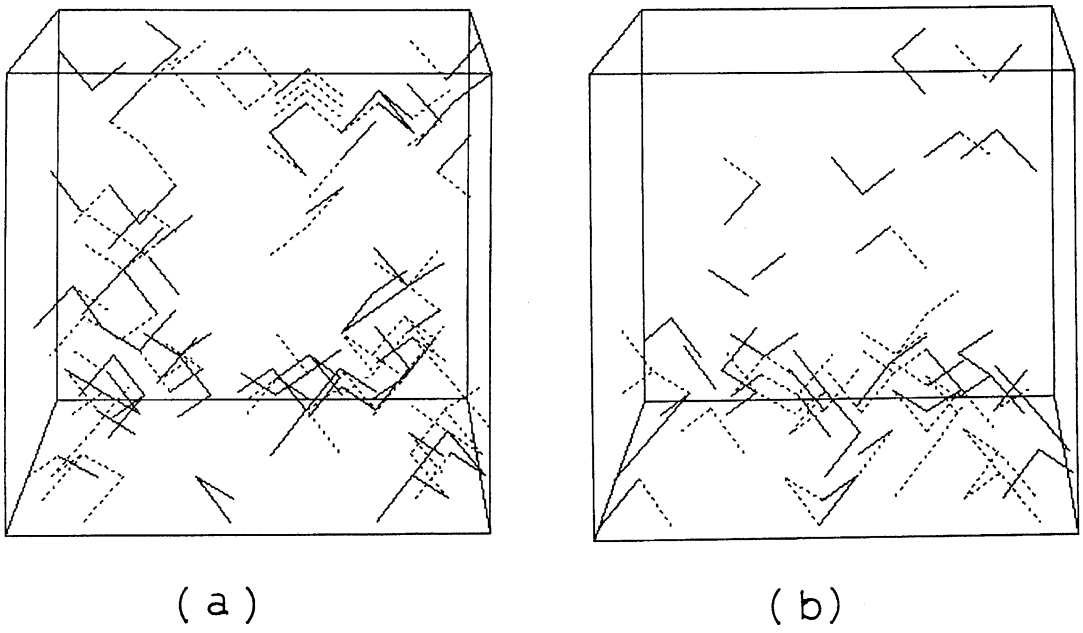


Fig. 15. Snapshots of the bond rearrangement patterns. Real lines are bonds newly formed during the $i$-th step and $i+20$ th step and dashed lines are bonds disconnected during the same period. $i=1900$ (a) and $i=2080$ (b). $T/B=0.1$ and the lattice size, the number of molecules and energy parameters are same as in Fig. 12. Regions of active rearrangement are localized in space. The 1-dim. string like region is seen in (a).

features of the network were studied and it was shown that bond rearrangement occurs collectively in localized regions. Further intensive study is necessary to reveal the statistical law for the network structural changes and their relations to the energy fluctuation and other experimentally observable fluctuations.

Thus the lattice-random-graph model of the hydrogen-bond network developed in this paper is an important tool to investigate the unsolved problems of liquid water. Many dynamical and thermodynamic features of water are still left unexplained and these water problems must be solved by further developing new methods; new concepts should await in the research of liquid water.

This work is supported by the Grant-in-Aid for the Priority Research Area of Chemical Reaction Theories from Ministry of Education, Science and Culture. The author thanks Drs. S. Sastry and F. Sciortino for sending him their manuscript prior to the publication. This paper is dedicated to the memory of Professor H. Kato.

## Appendix

The grand canonical partition function is written as

$$\Xi = \sum_{\{\sigma_i\}} \exp\left(\left(-H_{\text{non-HB}} + \mu \sum_i \sigma_i\right) \Big/ kT\right) Z(T, \{\sigma_i\}), \tag{A1}$$

and

$$Z(T, \{\sigma_i\}) = \exp\left(-\Psi(T, \{\sigma_i\})/kT\right) = \sum_{\{s_{ij}\}} \exp\left(-\left[H_{\text{CB}} + H_{\text{HB}}\right]/kT\right). \tag{A2}$$

We assume that $A$ in Eq. 4 is large enough, so that the condition $\Sigma_j s_{ij} = 2\sigma_i$ is always satisfied. Then Eq. A2 is approximately written in the following way:

$$Z(T, \{\sigma_i\}) = \prod_i Z_i(T, \{\sigma_i\}), \tag{A3}$$

and

$$Z_i(T, \{\sigma_i\}) = \sum_{\{s_{ij}\}} \prod_j{}' \{\sigma_i\sigma_j \times \exp\left(-\left[-Bs_{ij} + Cs_{ij}\langle s_{ji}\rangle\right]/kT\right) + (1 - \sigma_i\sigma_j)\}, \tag{A4}$$

where the product with prime is the product for nearest neighbor sites of $i$. and $<s_{ji}>$ is the average of $s_{ji}$ under the condition of $\sigma_i\sigma_j s_{ij}=1$. At high temperature $s_{ji}$ and $s_{ij}$ have no correlation, so that $<s_{ji}>=1/4$. At low temperature, on the other hand, $<s_{ji}>$ should be very small. We adopt the following form of $<s_{ji}>$ which connects 1/4 and 0:

$$\langle s_{ji}\rangle = \frac{1}{4}\exp\left(-\left(B - C\right)/kT\right). \tag{A5}$$

Then, Eq. A4 is

$$\begin{aligned} Z_i = {} & \left(\frac{8!}{2!6!}\exp(2D)\right)\sigma_i \prod_j{}'\sigma_j \\ & + \left(\frac{7!}{2!5!}\exp(2D) + 7\exp(D)\right) \\ & \times\sigma_i \sum_j{}'(1 - \sigma_j) \prod_{k(\neq j)}{}'\sigma_k \\ & + \left(\frac{6!}{2!4!}\exp(2D) + 2\times 6\exp(D) + 1\right) \end{aligned}$$

$$
\begin{aligned}
&\times\sigma_i \sum_{j,l}{}'(1-\sigma_j)(1-\sigma_l) \prod_{k(\neq j,l)}{}'\sigma_k \\
&+ \left(\frac{5!}{2!4!}\exp(2D) + 3\times 5\exp(D) + \frac{3!}{2!1!}\right) \\
&\quad\times\sigma_i \sum_{j,l,m}{}'(1-\sigma_j)(1-\sigma_l)(1-\sigma_m) \prod_{k(\neq j,l,m)}{}'\sigma_k \\
&+ \cdots \\
&+ \left(\frac{8!}{2!6!}\right)\sigma_i \prod_j{}'(1-\sigma_j) \\
&+ (1-\sigma_i), \qquad \text{(A6)}
\end{aligned}
$$

where $D=(B-C<s_{ji}>)/kT$. The first term of Eq. A6 expresses the case when the $i$-th site and its nearest neighbor sites are all occupied by molecules, the second term is when one of the nearest neigbors of $i$ is unoccupied, the third two of them are unoccupied $\cdots$, the ninth all of the nearest neighbors are unoccupied, and tenth, the last term is the case the $i$-th site is unoccupied. Summing up all the terms, Eq. A6 can be written in the compact form:

$$
\begin{aligned}
Z_i &= \sigma_i\left\{\frac{1}{2}\left(e^D-1\right)^2 \sum_j{}'\sum_l{}'\sigma_j\sigma_l \right. \\
&\quad \left. + \frac{15}{2}\left(e^D-1\right)\sum_j{}'\sigma_j + 28\right\} + (1-\sigma_i) \\
&= \exp\left\{\sigma_i \log\left(\frac{1}{2}\left[\left(e^D-1\right)\sum_j{}'\sigma_j + 8\right]\right.\right. \\
&\quad \left.\left.\times\left[\left(e^D-1\right)\sum_j{}'\sigma_j + 7\right]\right)\right\} \qquad \text{(A7)}
\end{aligned}
$$

From Eqs. A2, A3, A4, A5, and A7, we have

$$
\begin{aligned}
&\Psi(T,\{\sigma_i\}) = -kT\sum_i \sigma_i \\
&\quad\times\log\left\{\frac{1}{2}\left[8+\chi\sum_j{}'\sigma_j\right]\left[7+\chi\sum_j{}'\sigma_j\right]\right\}, \qquad \text{(A8)}
\end{aligned}
$$

and

$$
\chi = \exp\left\{\frac{1}{kT}\left[B-(C/4)\exp\left(\frac{B-C}{kT}\right)\right]\right\} - 1. \qquad \text{(A9)}
$$

These are Eqs. 10 and 11.

## References


1) H. Tanaka and I. Ohmine, *J. Chem. Phys.*, **87**, 6128 (1987).

2) M. Sasai, I. Ohmine, and R. Ramaswamy, *J. Chem. Phys.*, **96**, 3045 (1992); M. Sasai, in "Slow Dynamics in Condensed Matter," ed by K. Kawasaki et al., American Inst. Phys., New York (1992), p. 513.

3) F. Sciortino, P. H. Poole, H. E. Stanley, and S. Havlin, *Phys. Rev, Lett.*, **64**, 1686 (1990).

4) A. Geiger, F. H. Stillinger, and A. Rahman, *J. Chem. Phys.*, **70**, 4185 (1979).

5) H. E. Stanley and J. Teixeira, *J. Chem. Phys.*, **73**, 3404 (1980).

6) I. Ohmine, H. Tanaka, and P. G. Wolynes, *J. Chem. Phys.*, **89**, 5852 (1988); I. Ohmine and H. Tanaka, *J. Chem. Phys.*, **91**, 6318 (1989); **93**, 8138 (1990).

7) I. Ohmine and M. Sasai, *Prog. Theor, Phys., Suppl.*, **103**, 61 (1991).

8) C. A. Angell, "Water: A Comprehensive Treatise," ed by F. Franks, Plenum, New York (1982), Vol. 7, p. 1; *Annu. Rev. Phys. Chem.*, **34**, 593 (1983); *Nature*, **331**, 206 (1988).

9) R. J. Speedy, *J. Phys. Chem.*, **86**, 982 (1982).

10) P. H. Poole, F. Sciortino, U. Essman, and H. E. Stanley, *Nature*, **324** (1992); J. L. Green, D. J. Durben, G. H. Wolf, and C. A. Angell, *Science*, **249**, 649 (1990).

11) J. Hertz, A. Krogh, and R. G. Palmer, "Introduction to the Theory of Neural Computation," Addison-Wesley, New York, (1991); M. Mezard, G. Parisi, and M. A. Virasoro, "Spin Glass Theory and Beyond," World Scientific, New Jersey (1987).

12) J. J. Hopfield and D. W. Tank, *Biological Cybernetics*, **52**, 141 (1985); *Science*, **233**, 625 (1986).

13) S. Kirkpatrick, C. D. Gelatt, Jr., and M. P. Vecchi, *Science*, **220**, 671 (1983).

14) M. Mezard and G. Parisi, *J. Phys. (Orsay, Fr.)*, **46**, L-771 (1985); **49**, 2019 (1988).

15) Y. Fu and P. W. Anderson, *J. Phys. A*, **A19**, 1605 (1986).

16) G. M. Bell, *J. Phys. C*, **C5**, 889 (197); G. M. Bell and D. A. Lavis, *J. Phys. A*, **A3**, 427 (1970).

17) O. Weres and S. A. Rice, *J. Am. Chem. Soc.*, **94**, 8983 (1972).

18) P. D. Fleming, III and J. H. Gibbs, *J. Stat. Phys.*, **10**, 351 (1974).

19) J. S. Whitehouse, N. I. Christon, D. Nicholson, and N. G. Paronage, *J. Phys. A*, **A17**, 1671 (1984).

20) S. Sastry, F. Sciortino, and H. E. Stanley, to be published in *J. Chem. Phys.*

21) S. S. Borick and P. G. Debenedetti, *J. Phys. Chem.*, **97**, 6292 (1993).

22) D. Eisenberg and W. Kauzmann, "The Structure and Properties of Water," Oxford Press, London (1969).

23) R. E. Goldstein and J. S. Walker, *J. Chem. Phys.*, **78**, 1492 (1983); R. E. Goldstein, *J. Chem. Phys.*, **79**, 4439 (1983); J. S. Walker and C. A. Vause, *Phys. Lett. A*, **A79**, 421 (1980).

24) M. C. D'Antonio and P. G. Debenedetti, *J. Chem. Phys.*, **86**, 2229 (1987); P. G. Debenedetti and M. C. D'Antonio, *J. Chem. Phys.*, **84**, 3339 (1986).

25) M. Sasai, *J. Chem. Phys.*, **93**, 7329 (1990).

26) M. Sasai to be published.

27) F. H. Stillinger and T. A. Weber, *Phys. Rev. A*, **A25**, 978 (1982); *J. Phys. Chem.*, **87**, 2833 (1983); *Science*, **225**, 983 (1984).

28) Y. Oono and S. Puri, *Phys. Rev. A*, **A38**, 434 (1988); S. Puri and Y. Oono, *Phys. Rev. A*, **A38**, 1542 (1988).

29) P. Dutta and P. M. Horn, *Rev. Mod. Phys.*, **53**, 497 (1981); M. B. Weissman, *Rev. Mod. Phys.*, **60**, 537 (1988).